TEM study of defects versus growth orientations in heavily boron-doped diamond

F Lloret, D Araujo, M.P. Alegre, J.M. Gonzalez-Leal, M.P. Villar, D. Eon, E. Bustarret

TEM study of defects versus growth orientations in heavily boron-doped diamond

F. Lloret[1,2], D. Araujo[1], M.P. Alegre[1], J.M. Gonzalez-Leal[3], M.P.Villar[1], D. Eon[4], and E. Bustarret[4]

[1]Dpto. Ciencias de los Materiales, Universidad de Cádiz, 11510 Puerto Real, Cádiz, Spain.

[2]Institute of Electronic Structure and Laser, FORTH, 1385, Vassilika Vouton, Heraklion, Greece

[3]Dpto. Física de la Materia Condensada, Universidad de Cádiz, 11510 Puerto Real. Cádiz, Spain.

[4]Institut Néel, CNRS, 25 Avenue des Martyrs, BP 166, 38042 Grenoble, France.

Received ZZZ, revised ZZZ, accepted ZZZ
Published online ZZZ (Dates will be provided by the publisher.)

Keywords Diamond; CVD; Heavily boron-doped diamond; defects; TEM.

Heavy boron doping layer in diamond can be responsible for the generation of extended defects during the growth processes [1]. As claimed recently [2], boron pair interactions rather than strain related misfit seems to be responsible for such dislocation generation.

In the present work, electron microscopy observations are used to study the defects induced by heavy boron doping in different growth plane orientations. Facets of pyramidal Hillocks (PHs) and pits provide access to non-conventional growth orientations where boron atoms incorporation is different during growth. TEM analysis on FIB prepared lamellas confirm that also for those growth orientations, the generation of dislocations occur within the heavily boron-doped diamond layers. Stacking faults (SFs) have been also observed by high resolution transmission electron microscopy (HREM). From the invisibility criteria, using weak beam (WB) observation, $1/2\,[1\bar{1}0]$ and $1/6\,[11\bar{2}]$ Burger vectors have been identified. Their generation behavior confirms the mechanism reported by Alegre et al. [2] where local in-plane strain effects induced at the growing surface of the diamond lattice by the neighboring of several boron atoms cause the generation of such extended defects.

1 Introduction Synthetic diamond is known as a promising material for high power electronic devices due to its exceptional properties [3]. However, electronic devices require metallic diamond, getting it by doping. In fact, when boron concentration in diamond increases up to $5x10^{20}$atm/cm^3, their properties change drastically from an insulating behavior to a metallic one [4]. Unfortunately homoepitaxial boron doped layer usually contain planar and one-dimensional defects [5,6]. The origin of these defects is not well understood yet but they have an undesirable impact on the posterior diamond based devices [7,8]. The understanding of the mechanism of defects generation during the heavily boron doped diamond growth and its relationship to boron incorporation will help to understand and to improve the boron-doped diamond growth. This is one of the required technological steps to develop well designed commercial electronic devices.

Under these premises, Alegre et al. [2] reported an original mechanism of dislocations generation that established a critical boron-doping levels in diamond. In line with that work, an extensive study of defects in heavily boron-doped layers for different growth planes orientations is presented here.

2 Experimental In order to determine where defects occur, within the heavily doped layer or at interfaces with the substrate or with a layer of different doping level, as well as its relationship with the layer thickness, a multilayer structure has been studied. Therefore, under exactly the same growing conditions summarized in *table 1*, a stack of nine undoped and heavily boron-doped (10^{20} at/cm^3) diamond bilayers was grown by microwave plasma chemical vapor deposition (MPCVD) on a <100> oriented polished CVD diamond 3x3 mm^2 substrate. An initial 2h-long pure

hydrogen plasma was used to eliminate residual contamination Similar to a previous work [9], methane concentration of 0.5% in purified H_2 was then used to grow the nine boron doped layers with 7000 ppm B_2H_6/CH_4. After a short hydrogen flush, the CH_4/H_2 ratio was raised to 0.75% and oxygen added during the nominally undoped growth. Substrate temperature and pressure were kept at 910ºC and 33 Torr throughout the growth without interrupting the plasma.

Table 1 Summary of the growth conditions of the studied sample (stack of nine bilayers).

Non intentionally doped		**Boron doped p^{++}**	
CH_4/H_2 (%)	0.75	CH_4/H_2 (%)	0.5
O_2/H_2 (%)	0.32	B_2H_6/CH_4 (ppm)	7000
Flow rate (sccm)	200	Flow rate (sccm)	200
Pressure (Torr)	33	Pressure (Torr)	33
Time (min)	11.8	Time (min)	11.3
T_{sub} (ºC)	910	T_{sub} (ºC)	910
H_2 Flush duration (sec)		10	
Flow rate H_2 flush (sccm)		2000	

Focused ion beam-prepared lamellas have been obtained for cross sectional transmission electron microscopy (TEM) observations using a dual beam FEI QUANTA 200 3D microscope and following the lift-out method [10]. TEM diffraction contrast study was realized with a 120kV JEOL 1200 EX microscope and high resolution TEM observation with a 200kV JEOL 2010F microscope.

3 Results and discussion Fig. 1 shows weak beam (WB) micrographs in two beam conditions for two different reflections (g=022 and g=111) recorded at the [011] pole of the sample. This region presents a high density of defects. For an easier identification, doped layers have been marked by arrows with p^{++} labels. From the orientation of the lamella planes and the angles observed in the micrographs, the growth plane facet orientations are deduced (see dashed lines in Fig. 3d). First observation is that the <111> facets of the triangular shaped pit defects on the substrate (probably coming from etching before CVD-growth) induce the <111> growing orientation of the first p^{++} layers and also for first nanometres of the underneath layer (undoped buffer layer) undoped layer, instead of the expected <100> growing. That is, growing orientation is clearly conditioned by the existence of superficial defects on the substrate. As is shown in micrographs, extended defects are generated in (111) growth plane of the first doped layer becoming parallel to the <100> growing orientation some nanometres later on.

Dislocations coming from strain related or lattice mismatch usually occur at the interface between doped and undoped layers [11]. However, Fig. 2 shows an annular dark field (ADF) micrograph, recorded at 20 cm camera leght, where dislocations are generated at different positions with respect to the doped layers.

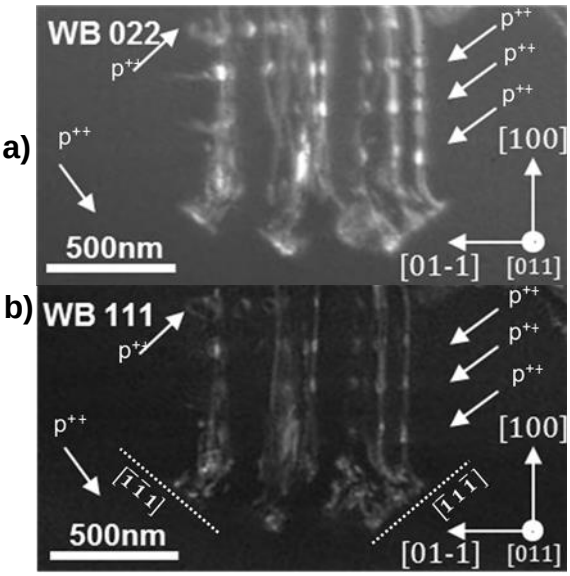

Figure 1 Weak beam micrographs in two beam conditions for the 022 (a) and 111 (b) reflections. Doped layers are marked by arrows and p^{++} label. Plane of growth where the defects are generated are marked by dashed lines in (b) and corresponds with $[\bar{1}\bar{1}1]$ and $[\bar{1}1\bar{1}]$.

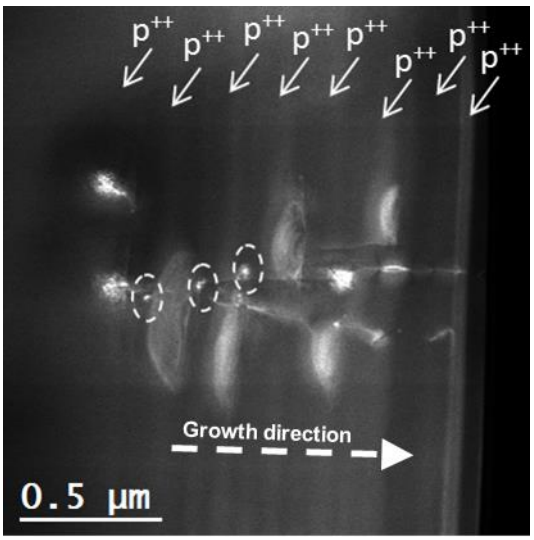

Figure 2. Annular dark field (ADF) micrograph recorded at 20cm camera length where defects marked by white dashed circles are placed at diferent position of the boron-doped layers. White arrows and p^{++} labels show doped layers.

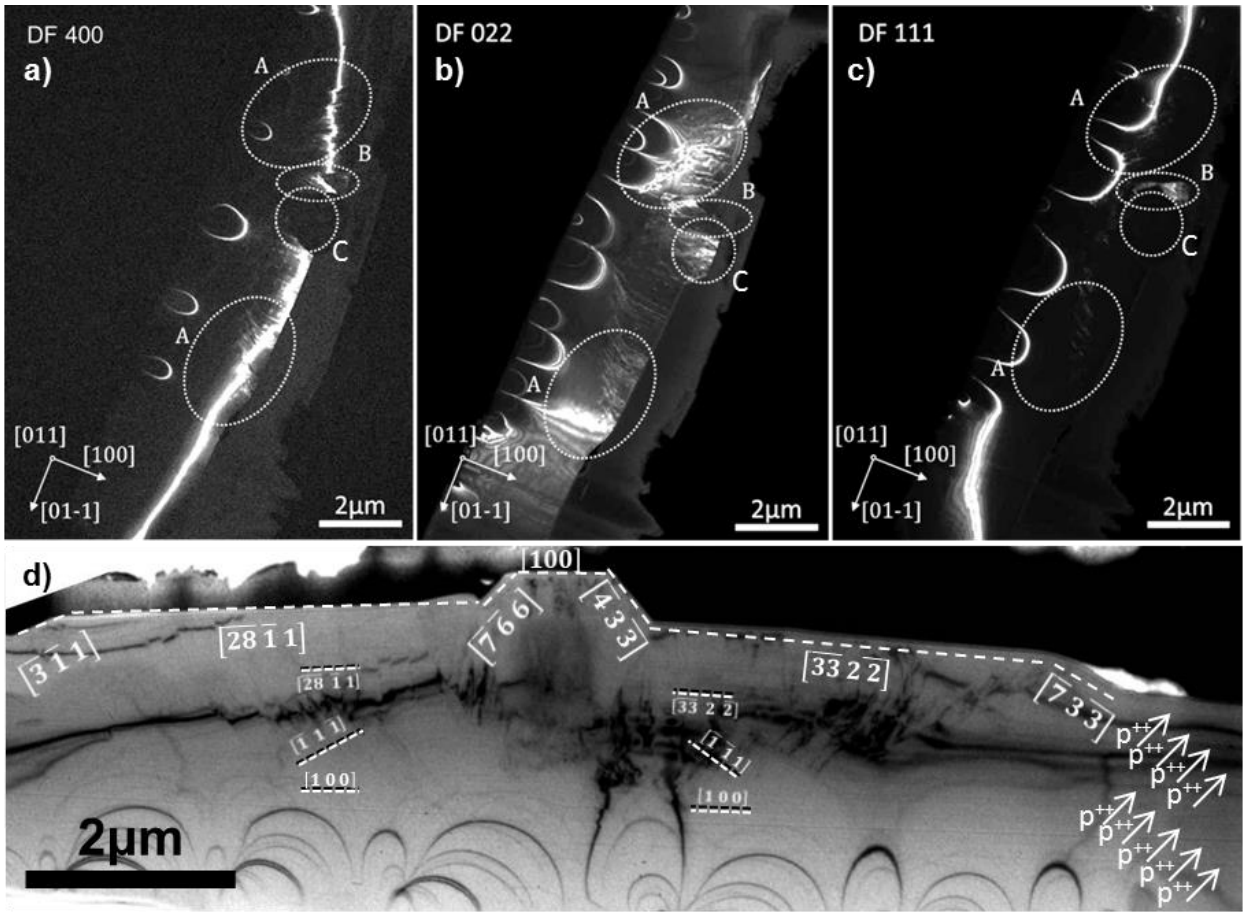

Figure 3. Dark field micrographs in two beam conditions for (a) **g**=400, (b) **g**=022 and (c) **g**=111 reflections of a cross section of a pyramidal hillock (PH). Groups of defects are encircled and labeled according with its Burger vector, "A" defects correspond to $\boldsymbol{b} = \pm\frac{1}{6}[11\bar{2}]$ and "B" ones to $\boldsymbol{b} = \pm\frac{1}{2}[1\bar{1}0]$. (d) Bright field micrograph of the PH whose different growth orientations are marked by white dashed lines and identified by labels. Doped layers are marked by arrows and p^{++} labels. They show different orientation during growth. Six of these intermediate growth directions are indicated by white/black dashed lines where they are revealed by the doped layers and planes are identified by labels.

In order to confirm this behaviour, different orientations have been compared. For this purpose, 3D-superficial defects generated during the growth process have been used.Growth defects such as pyramidal hillocks (PH) or flat hillocks (FH) are commonplace on the surface of epitaxial diamond samples growth by CVD [12]. The formation of these defects has been thorough studied by authors as A. Tallaire et al. [13] who attributed their formation to a crystalographic defect. Although the defect at the source of the PH could not be identified here, due the conditions of our experiments and the similarities between the ones studied by Tallaire and the one here studied, we assumed that the same mechanisms take place during the formation of the PH studied. Fig. 3 shows dark field (DF) micrographs of the PH in two beam conditions for g=400 (Fig. 3a), g=022 (Fig. 3b) and g=111 (Fig. 3c) reflections. Images have been recorded at [011] pole. PH had a squared shaped base with their side parallel to the $\langle 011\rangle$ and $\langle 0\bar{1}1\rangle$ directions. As expected, each face of the hillock shows different growth direction at the surface of the sample. They have been identified and marked in the bright field (BF) micrograph presented in Fig. 3d. The high density of defects generated at initial growth planes is shown in DF micrographs. Three different regions of defects have been identified and they have been marked by white dashed circles. Doped layers show multiple growth orientations during PH formation. These changes in the growth directions curved the dislocation lines. Fig. 3d shows that growth orientation changed at least twice per edge during the PH generation. $(\overline{28}\ \bar{1}\ 1)$ and $(\overline{33}\ 2\ \bar{2})$ planes started to grow following the <100> direction. After around 400nm, the growth orientation changed to the $\langle\bar{1}\ \bar{1}\ 1\rangle$ and $\langle\bar{1}\ 1\ \bar{1}\rangle$, respectively. In fact, the dislocations density, defined as sum of the dislocations length per volume:

$$\rho = \frac{\sum \text{dislocation length}}{volume}, \quad (1)$$

has been calculated for each one of the growth planes

identified in the sample. A higher density of dislocations was obtained for the (111) family planes. This situation confirms the particular afinity of defects to be generated in (111) planes against any other less packed plane orientation, showing that the distance between atoms is the main reason of its formation.

In order to identify the Burger vectors and to determine the family of defects observed in the micrograph, invisibility criterion has been employed. It is well known [14] that the visibility of edge dislocations observed in TEM is complicated by the strain field component normal to the slip plane for edge dislocations. Consequently, complete invisibility of edge dislocations is only achieved under conditions of $\mathbf{g}\cdot\mathbf{b}=0$ where $\mathbf{g}$ is the normal to the TEM diffracting planes and $\mathbf{b}$ is dislocations burger vector. *Table 2* shows the result of applying this criterion ($\mathbf{g}\cdot\mathbf{b}=0$) for the reflections used in this work (g=220, g=111 and g=400) which allows to determine the burger vector orientations along <011> direction.

Fig. 4 shows weak beam (WB) micrographs in two beam conditions in the same region of the sample recorded at Fig. 2. Micrographs were recorded at the [011] pole for three reflections: g=220 (Fig. 4a), g=111 (Fig. 4b) and g=400 (Fig. 4c). Defects with $\boldsymbol{b} = \pm\frac{1}{6}[11\bar{2}]$, marked with label "A", and $\boldsymbol{b} = \pm\frac{1}{2}[1\bar{1}0]$, marked with label "B", have been observed. Similar dislocations have been previously reported [15].This criterion has been used also for dislocations contained in Fig. 3 where the same Burger vectors were observed. They are also marked with labels "A" and "B" in the corresponding micrographs.

Table 2 Results of the $\boldsymbol{g}\cdot\boldsymbol{b}$ invisibility criterion for the usually observed Burger vectors (b) using the reflections (g) present at the 110 pole. The shadows and the letters "A" and "B" remark the cases corresponding with the results from the micrographs.

	b \ g	$(\mathbf{400})$	$(\mathbf{0\bar{2}2})$	$(\mathbf{11\bar{1}})$
A	$\pm\frac{\mathbf{1}}{\mathbf{6}}[\mathbf{11\bar{2}}]$	$\pm\frac{2}{3}$	±1	$\pm\frac{2}{3}$
	$\pm\frac{\mathbf{1}}{\mathbf{6}}[\mathbf{121}]$	$\pm\frac{2}{3}$	$\pm\frac{1}{3}$	$\pm\frac{1}{3}$
	$\pm\frac{\mathbf{1}}{\mathbf{6}}[\mathbf{211}]$	$\pm\frac{4}{3}$	0	$\pm\frac{1}{3}$
	$\pm\frac{\mathbf{1}}{\mathbf{3}}[\mathbf{111}]$	$\pm\frac{4}{3}$	0	$\pm\frac{1}{3}$
	$\pm\frac{\mathbf{1}}{\mathbf{2}}[\mathbf{101}]$	±2	±1	0
	$\pm\frac{\mathbf{1}}{\mathbf{2}}[\mathbf{10\bar{1}}]$	±2	±1	±1
	$\pm\frac{\mathbf{1}}{\mathbf{2}}[\mathbf{011}]$	0	0	0
	$\pm\frac{\mathbf{1}}{\mathbf{2}}[\mathbf{01\bar{1}}]$	0	±2	±1
	$\pm\frac{\mathbf{1}}{\mathbf{2}}[\mathbf{110}]$	±2	±1	±1
B	$\pm\frac{\mathbf{1}}{\mathbf{2}}[\mathbf{1\bar{1}0}]$	±2	±1	0

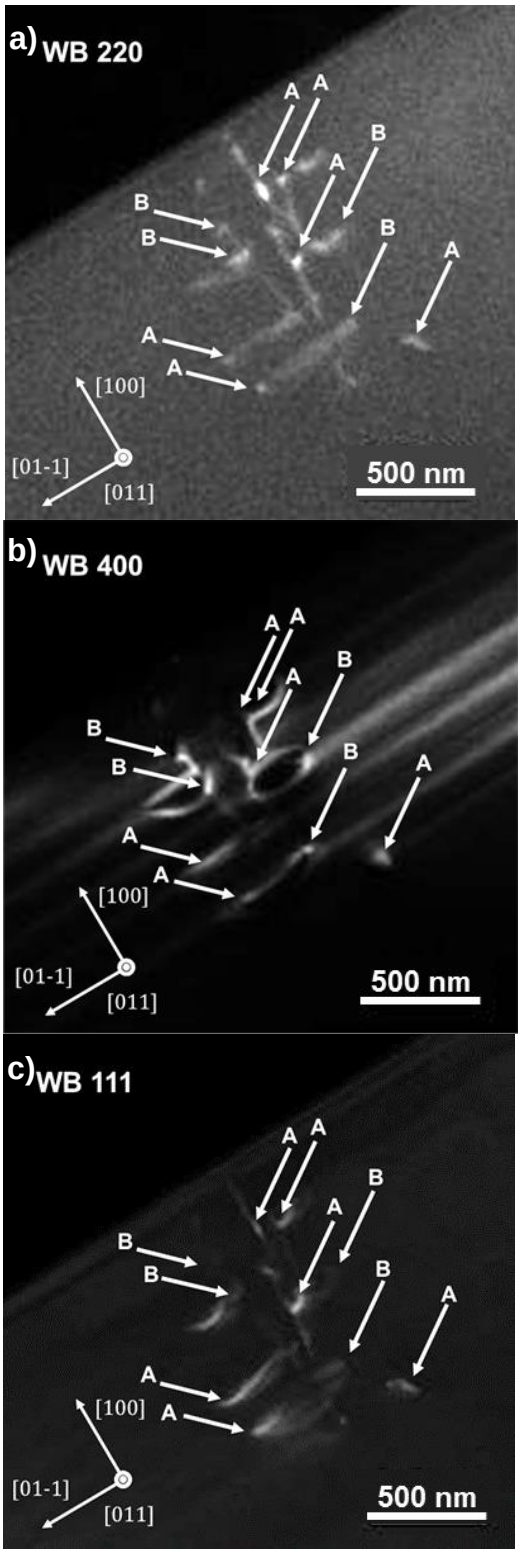

Figure 4 Weak beams micrographs under two beam conditions for the 220 (a), 400 (b) and 111 (c) reflections. Arrows and labels are used to identify the defects. "A" corresponds to a $1/6\left[\,11\bar{2}\right]$ Burger vector and "B" with $1/2\,[1\bar{1}0]$ one. Doped layers are mainly observed for reflexion 400.

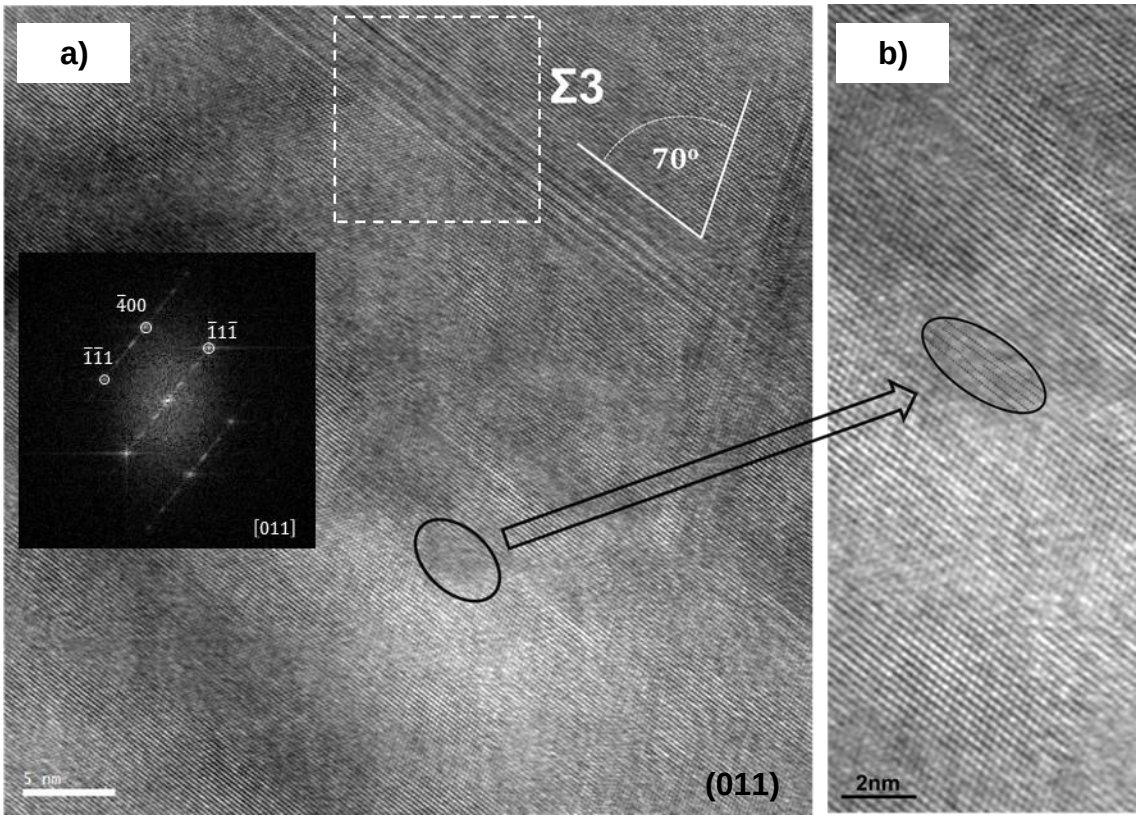

Figure 5 HREM micrographs recorded at the [011] pole of sample growth in 100 direction. Planar defects such as stacking faults (SFs) as well as dislocations are showed. SFs show to form an angle close to 70º consistent with the ∑3 type in the CSL model. Inset Fourier transform, corresponding to the white dashed square in (a), demonstrated that SFs are {111} type. Also some dislocations were observed. Enlarged in figure (b) a threading edge dislocation is shown.

Fig. 5 shows a high resolution transmission electron microscopy (HREM) micrograph of a doped region of the sample recorded at the [011] pole. Stacking faults are observed forming an angle of 70.53º. As previously reported [16], these planar defects correspond with the ∑3 coincident-size-lattice structure. In addition, a Fourier transform performed on the defects (white dashed square on Fig. 5a) shows that they correspond to the {111} type. These structures are twins boundaries-like and they have been observed in polycrystalline diamond [17, 18]. Preferred grain boundary planes are the closest packed planes of the corresponding CSL that is, (111) planes. Here, an additional observation of the preferential planes for extended defects generations is shown.

Edge dislocations were also observed by HREM as shown in Fig. 5a and 5b at higher magnification. In this case it corresponds to a threading edge dislocation with a $1/2\,[1\bar{1}0]$ Burger vector.

In correspondence with the dislocation generation model published by M. P. Alegre et al. [2], the following aspects are observed: (i) in plane dislocations (Fig. 4b and 5) are generated exclusively insight the heavily doped layer, (ii) such dislocations (observed as points) changes then their orientation to follows the growth directions.

In general, regions of the sample where the growth plane is along the <100> direction are almost free of defects. Therefore, a special tendency to generate defects at (111) growth plane in opposition to <100> orientation with exactly the same growth conditions is evidenced. This behaviour is in according with the mechanism reported by Alegre [2]. Neighbouring effects between boron atoms might be higher for (111) family planes than for (100) since these (111) planes have smaller planar distance. Local strains due the distance between the substitutional boron pairs and their neighbours have a higher influence on the generation of dislocations than interface strain related effects [2, 15].

4 Conclusions Highly boron-doped diamond epilayers grown along <100> direction have been characterized by TEM. Additional growth directions have been also characterized thanks to local changes in the growth directions

due the presence of etch-pits at the initial stage of growth and pyramidal hillock formed during the growth. A large number of defects have been obtained along the <111> growth direction, in contrast with other directions using the same growth conditions. In this way, the dependence of the dislocation generation on the growth orientation has been shown. Threading dislocations observed had $1/6\left[11\bar{2}\right]$ and $1/2\,[1\bar{1}0]$ Burger vectors and stacking faults with the structure Σ3 {111} coincident-site-lattice (CSL) have been identified.

All these results are consistent with the model proposed by Alegre et al. [2].

Acknowledgements F. Lloret would like to acknowledge Prof. K. Zekentes for his financial support by the European project LAST-POWER (2009SE01380012, Program ENIAC, GSRT). Authors are also grateful for the project TEC2009-11399 of the Spanish Government.

References

[1] V. D. Blank, V. N. Denisov, A. N. Kirichenko, M. S. Kuznetsov, B. N. Mavrin, S. A. Nosukhin, and S. A. Terentiev, Diamond Relat. Mater. **17**, 1840 (2008).

[2] M. P. Alegre, D. Araújo, A. Fiori, J. C. Pinero, F. Lloret, M. P. Villar, P. Achatz, G. Chicot, E. Bustarret, and F. Jomard, Appl. Phys. Lett. **105**, 173103 (2014).

[3] R. S. Balmer, J. R. Brandon, S. L. Clewes, H. K. Dhillon, J. M. Dodson, I. Friel, P. N. Inglis, T. D. Madgwick, M. L. Markham, T. P. Mollart, N. Perkins, G. A. Scarsbrook, D. J. Twitchen, A. J. Whitehead, J. .J. Wilman, and S. M. Woollard, J. Phis.: Condens. Matter **21**, 364221 (2009).

[4] E. Bustarret, P. Achatz, B. Sacépé, C. Chapelier, C. Marcenat, L. Ortega, and T. Klein, Phil. Trans. R. Soc. A **366**,267 (2008).

[5] D. Araújo, E. Bustarret, A. Tajani, P. Achatz, M. Gutiérrez, A. J. García, and M. P. Villar, Phys. Status Solidi A **207**, 2023 (2010).

[6] I. A. Prokhorov, V. G. Ralchenko, A. P. Bolshakov, A. V. Polskiy, A. V. Vlasov, I. A. Subbotin, K. M. Podurets, E. M. Pashaev, and E. A. Sozontov, Crystallogr. Rep. **58**, 1010 (2013).

[7] K. S. Siegert, F. R. L. Lange, E. R. Sittner, H. Volker, C. Schlockermann, T. Siegrist, and M. Wuttig, Rep. Prog. Phys. **78**, 013001 (2015).

[8] J. Alvarez, M. Boutchich, J. P. Kleider, T. Teraji, and Y. Koide, J. Phys. D: Appl. Phys. **47**, 355102 (2014).

[9] A. Fiori, J. Bousquet, D. Eon, F. Omnès, E. Bellet-Amalric, E. Bustarret, Appl. Phys. Lett. **105**, 081109 (2014).

[10] P. Olivero, S. Rubanov, P. Reichart, B. C. Gibson, S. T. Huntington, J. Rabeau, A. D. Greentee, J. Salzman, D. Moore, D. N. Jamieso, and S. Prawer, Adv. Mater. **17**, 2430 (2005).

[11] S. Kitagoh, R. Okada, A. Kawano, M. Watanabe, Y. Takano, Y. Yamaguchi, T. Chikyow, and H. Kawarada, Phys. C **470**, S610 (2010).

[12] H. Sawada, H. Ichinose, H. Watanabe, D. Takeuchi, and H. Okushi, Diamond Relat. Mater. **10**, 2030 (2001).

[13] A. Tallaire, M. Kasu, K. Ueda, and T. Makimoto, Diamond Relat. Mater. **17**, 60 (2008).

[14] D. B. Williams, and C. B. Carter, Transmission Electron Microscopy, Springer, New York, 1996

[15] J. W. Matthews, and A. E. Blakeslee, J. Cryst. Growth **27**, 118, (1974).

[16] Y. Zhang, H. Ichinose, M. Nakanose, K. Ito, and Y. Ishida, J. Electron Microsc. **48**, 245 (1999).

[17] H. Sawada, H. Ichinose, H. Watanabe, D. Takeuchi, and H. Okushi, Diamond Relat. Mater. **10**, 2096 (2001).

[18] Y.-G. Lu, S. Turner, J. Verbeeck, S.D. Janssens, P. Wagner, K. Haenen, G. van Tendeloo, Appl. Phys. Lett. 101, 041907 (2012).